AIAA SciTech Forum
7-11 January 2019, San Diego, California
AIAA Scitech 2019 Forum

10.2514/6.2019-1144

A Comparison of Implicit and Explicit Simulations of Vortex Breakdown

Xiao Zhang *, Joseph D. Chung *, Carolyn R. Kaplan †, Elaine S. Oran ‡
Department of Aerospace Engineering, University of Maryland, College Park, MD, 20742

Vortex breakdown is an instability which occurs in swirling flows and is seen in both incompressible and compressible flow regimes. The choice of numerical algorithm to compute this flow is critical to resolving the relevant physical phenomena. In previous work, we described the procedure of combining a Barely Implicit Correction (BIC) algorithm with a fourth-order Flux-Corrected Transport (FCT) algorithm to eliminate the sound speed limit for explicit calculations of low-speed flows, and showed that BIC-FCT could predict the three major vortex breakdown modes (spiral, bubble and double-helix). Here, we show a direct comparison of the implicit BIC and explicit FCT algorithms by using the same time step within the explicit stability limit. The comparison is conducted on simulations of a three-dimensional, swirling jet flow with vortex breakdown, by examining the flow structures and examining the property fields. Differences are observed in the phase of the downstream spiral and double-helix modes. Based on a pressure wave analysis, we attribute this phase shift to the difference of how the explicit FCT and implicit BIC treat an open outflow boundary.

I. Introduction

Swirling flows are observed in nature as tornadoes, dust devils, hurricanes, and fire whirls. They are also used for technical applications such as the micro-bubble generator, swirl fuel injector, and gas turbine swirl burner. In these swirling flows, the swirl level (measured by the ratio of the azimuthal to axial velocity intensities) has significant effects on the vortex stability. When the swirl level is increased to a critical point, the adverse pressure gradient, which forms along the vortex axis, can be strong enough to overcome the axial momentum. The flow field then adjusts and reaches a new state with a stagnation point and a finite recirculation zone forming downstream around the jet centerline. This new state arising due to vortex breakdown has a strong effect on the ensuing fluid dynamics.

The types and result of vortex breakdown is described by flow structures seen in early experimental investigations. Sarpkaya's flow visualization[1,2] shows three types of vortex breakdown, each with a distinctive internal structure. These modes are the bubble, spiral, and the double-helix modes. They were identified visually by injecting dye into the center of the jet flow. These three modes are among the seven types of the vortex structures reported by Faler and Leibovich.[3] These include two intermediate states of the spiral mode, a smooth bubble mode, and a ragged bubble mode in addition to the three major ones above, all defined based on the flow visualizations through dye-filament injection. Another configuration observed by Billant et al.[4] is an open conical sheet.

Over the past few decades, extensive theoretical, numerical and experimental research has been performed on studying the onset and flow structure resulting from vortex breakdown. The three main theoretical approaches used have been: a failure of the Quasi-cylindrical approximation,[5] existence of a critical state,[6,7] and hydrodynamic instability.[8–10] Some combined and extended explanations have been proposed more recently since the early theories cannot independently and completely describe all the flow features.[11–14] There is, however, no generally accepted theoretical description of the evolved state.

*Graduate Research Assistant, Dept. of Aerospace Engineering, 3202 James M. Patterson Bldg., and AIAA Student Member.
†Research Associate Professor, Dept. of Aerospace Engineering, 3202 James M. Patterson Bldg., and AIAA Associate Fellow.
‡Glenn L. Martin Professor, Dept. of Aerospace Engineering, 3232 Jeong H. Kim Engineering Bldg., and AIAA Honorary Fellow.

Significant progress was made towards understanding vortex breakdown through numerical approaches. Due to computational constraints, early simulations assumed incompressible, laminar, axisymmetric and steady flows (e.g., Refs. 15, 16). Since the 1990s, a number of three-dimensional, incomrpessible, unsteady flow calculations were performed. For example, Spall et al.[17] demonstrated the inherent non-axisymmetrical internal structure of the bubble. Ruith et al.[18] computed all three major modes by systematically varying three governing parameters. Vortex breakdown was also studied in the compressible flow regime by recent simulations that looked at Mach number[19–21] and chemical-reaction[22,23] effects. Many of these compressible flow simulations, however, are confined to axisymmetric calculations due to the excessive computational cost.

Computation of the full 3D compressible Navier-Stokes equations for this low-speed flow is economically prohibitive when an explicit algorithm is used because numerical stability requires restricting the time step based on the sound speed. In the low-speed flow regime, the fluid velocities can be hundreds of time smaller than the sound speed. If the restriction on the time step from the sound speed were removed, the computational efficiency would be improved by one or two orders of magnitude. One approach to lower the computational cost is to make the time-integration implicit (e.g., Refs. 24–26). These methods are accurate but expensive; also, stability is often an issue. Another way is the asymptotic approach, which allows for pressure variation over time and filters out spatial pressure differences (see e.g., Refs. 27–32).

In a previous work,[33] we applied a Barely Implicit Correction (BIC)[34,35] to the fourth-order Flux-Corrected Transport (FCT)[36] algorithm. This approach solves one extra elliptic equation for an pressure correction to eliminate the sound speed restrictions in the time step. This method maintains a low computational cost per time step and preserves the effects of acoustic waves when needed. In 33, we demonstrated the ability of the implicit algorithm BIC-FCT to remove the sound-speed limit in the numerical time step for a three-dimensional flow with complex swirling motions and open boundaries. We also showed that BIC-FCT can predict the three major types of vortex breakdown when using large time steps without adhering to requirement based on the sound-speed limit.

In this paper, we compare the performance of BIC-FCT to the explicit FCT when using the same time steps within the explicit stability limit. We perform the comparison by simulating a three-dimensional, swirling jet flow with an open boundary using both methods. We show the flow undergoing all three major types of vortex breakdown. A qualitative comparison shows agreement between the explicit and implicit calculations on the vortical structures. Quantitative differences are observed in the phase of the downstream spiral and double-helix modes, which are further investigated and explained by comparison of the influence of pressure waves in both calculations.

II. Governing Equations

The formulation is based on the time-dependent, compressible Navier-Stokes equations:

$$\frac{\partial \rho}{\partial t} = -\nabla \cdot (\rho \mathbf{V}) \tag{1}$$

$$\frac{\partial (\rho \mathbf{V})}{\partial t} = -\nabla \cdot (\rho \mathbf{V}\mathbf{V}) - \nabla P - \nabla \cdot \hat{\tau} \tag{2}$$

$$\frac{\partial E}{\partial t} = -\nabla \cdot ((E+P)\,\mathbf{V}) - \nabla \cdot (\mathbf{V} \cdot \hat{\tau}) - \nabla \cdot (K \nabla T) \tag{3}$$

$$\hat{\tau} = \rho\nu \left(\frac{2}{3} (\nabla \cdot \mathbf{V})\,\mathbf{I} - (\nabla \mathbf{V}) - (\nabla \mathbf{V})^{\dagger} \right) \tag{4}$$

in which t is time, ρ is density, P is pressure, E is total energy, $\mathbf{V}$ is the velocity vector, T is temperature, K is thermal conductivity, I is the identity matrix. We consider Newtonian fluids for which $\hat{\tau}$ is the stress tensor as shown in Eq. (4) and ν is the kinematic viscosity. The superscript † denotes the matrix transpose. The total energy is calculated according to

$$E = \rho e + \frac{1}{2}\rho \mathbf{V}. \tag{5}$$

Here e is the specific internal energy computed as

$$e = \frac{P}{\rho(\gamma - 1)}, \tag{6}$$

which assumes a perfect, ideal gas using the ideal gas equation of state,

$$P = \rho \frac{R_u}{M_w} T. \tag{7}$$

III. Numerical Methods

The explicit numerical algorithm uses the LCPFCT[36] version of the FCT implementation with a fully multidimensional limiter by Zalesak[37] with a modification from DeVore.[38] The implicit algorithm combines the explicit FCT with BIC[33] to remove the sound-speed limit in the time step while maintaining the stability and accuracy. The BIC algorithm used here is a modified version based on both of the original approach in Ref. 34 and a later version in Ref. 35, by improving the numerical stability when diffusion processes are included. There are two main stages in the solution procedure. It starts with an explicit predictor step using a large time-step based on Courant-Friedichs-Levy (CFL) condition governed by the fluid velocity. Then it is followed by a implicit corrector step, which solves an elliptic equation for a pressure correction to equilibrate the acoustic waves. The details of the procedure are summarized in Ref. 33.

A time-step splitting procedure is adopted to couple the diffusion and the convection processes. This means the diffusion and convection fluxes are calculated serially in each time step. In both the explicit and the implicit simulations, the only difference is how the convective process is integrated; one uses an explicit FCT solver and the other uses an implicit BIC-FCT solver. The diffusion processes are integrated explicitly using the same second order Runge-Kutta method in both calculations.

A Cartesian mesh is employed with three levels of refinement. The mesh and refinement are based on the flow conditions and are therefore discussed together with the simulation setup in the following section.

IV. Simulation Results

Now we compute a three-dimensional, swirling, compressible flow undergoing vortex breakdown using both fully explicit FCT and the implicit BIC-FCT. Both the explicit and implicit simulations use a Grabowski vortex profile as an initial condition.[16,18] This vortex is defined by azimuthal, radial, and axial velocities as a function of the radial location r as

$$v_\theta(0 \leqslant r \leqslant 1) = S_w r(2 - r^2) \tag{8}$$

$$v_\theta(1 \leqslant r) = S_w / r \tag{9}$$

$$v_r(r) = 0 \tag{10}$$

$$v_z(0 \leqslant r \leqslant 1) = \alpha + (1 - \alpha) r^2 (6 - 8r + 3r^2) \tag{11}$$

$$v_z(1 \leqslant r) = 1. \tag{12}$$

Here the swirl number is $S_w = v_\theta(R)/v_{z,\infty}$, where R being the radius of the vortex core. The Reynolds number is defined as $Re = v_{z,\infty} R/\nu$. The flexibility of initializing a nonuniform axial velocity profile is given by the coflow parameter $\alpha = v_{z,c}/v_{z,\infty}$, which describes a jet-like profile when greater than unity and a wake-like profile when smaller than unity. We set $Re = 200$, $S_w = 1.3$, $\alpha = 1$, $R = 1$, and $v_{z,\infty} = 1$ m/s, which are also the conditions in simulations by Ruith et al.[18] In a swirling flow, the radial forces acting on a particle should be balanced by the centrifugal force pointing outwards and the pressure gradient force directed inwards. This force balance is shown in the following equation,

$$\frac{v_\theta^2}{r} = \frac{1}{\rho} \frac{\partial P}{\partial r}. \tag{13}$$

Based on this force balance, we derive the Grabowski pressure profile as a function of the radial location r. This profile consists of two regions: outside of the vortex core (Eq. 14), and inside of the vortex core (Eq. 15):

$$P_{out}(1 \leqslant r) = \rho S^2 \left(-\frac{1}{2r^2} \right) + P_\infty \tag{14}$$

$$P_{in}(0 \leqslant r \leqslant 1) = \rho S^2 \left[\frac{r^6}{6} - r^4 + 2r^2 - \frac{7}{6} \right] + P_{out}(r = 1). \tag{15}$$

The CFL condition is defined as:

$$\mathrm{CFL}_{\mathrm{wave}} = \frac{(\text{sound speed} + \text{fluid velocity}) \times \text{time step}}{\text{cell size}}. \tag{16}$$

Both of the explicit FCT calculation and the implicit BIC calculation are performed with $\mathrm{CFL}_{\mathrm{wave}} = 0.8$ for the detailed comparison in this paper. Note, however, that BIC is designed and is able to work at high $\mathrm{CFL}_{\mathrm{wave}}$, perhaps on the order of thousands.[33]

For the two cases shown in this work, the sound speed is scaled to maximize the time step, so that the computational cost is minimized. The scaling is performed by increasing the fluid density while keeping the Mach number below 0.15 to maintain the flow characteristics under the chosen configuration. In this procedure,

1. The maximum Mach number is defined as $M_{max} = v_{max}/a = v_{max}/\sqrt{\gamma P/\rho}$, where v_{max} is the maximum fluid velocity and a is the sound speed. In order to keep M_{max} below 0.15, we selected ρ to be 1000 kg/m^3 so that the resulted far-field pressure $P_\infty \approx 71428$ Pa, which is not too far from a realistic condition. The peak velocity magnitude v_{max} is obtained from the initial velocity field.

2. The molecular weight is chosen to be $M_w = 1000$ kg/kmol. The resultant temperature in the initial flow field is $T_{min} = 8.427$ K and $T_{max} = 8.573$ K, which is calculated using $T = PM_w/(R_u\rho)$.

Figure 1 shows the initial pressure and azimuthal velocity profiles, which are the same for both explicit and implicit calculations. A 40 m $\times$ 40 m $\times$ 20 m cubical domain is adopted for both calculations, as shown in Fig. 2. Here we refer to the z-axis as the axial direction. We set the lower axial x-y plane as an inflow boundary as indicated in Fig. 2, with the Grabowski vortex profile as described above. The pressure is controlled at the lateral boundaries using Bernoulli's equation, since the flow is assumed to be irrotational outside of the vortex core. This boundary pressure is then calculated by $P = P_\infty - \rho V^2/2$, where V is the magnitude of the velocity. The velocity at the lateral boundaries are specified using a first-order extrapolation with a zero gradient. For flow leaving the boundaries, we also apply the same first-order extrapolation with a zero gradient for the temperature. For flow coming into the boundary, we specify the temperature using the ideal gas law with the fixed density discussed earlier. The upper axial x-y plane is set as non-reflecting.

The flow is initialized with the axisymmetric, columnar Grabowski vortex profile throughout the whole domain, in which the axisymmetry is applied at the center of the x-y plane along the z axis. A Cartesian mesh is employed with three levels of refinement. The cell width is halved for each level. In Fig. 2, we show that the coarsest mesh has 128 cells in the x and y directions, 144 cells at the second level, and 168 cells at the finest level. The refinement selected initially is not allowed to change during the calculation. The radial location of refinement is fixed at where the radial pressure gradient is not significant based on Eqs. (14) and (15).

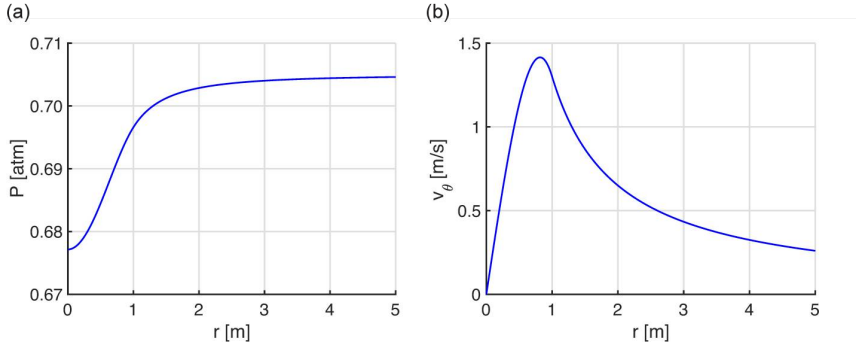

Figure 1. Grabowski vortex profile with $S = 1.3$, $\alpha = 1$: (a) Pressure distribution for the Grabowski vortex profile; (b) Azimuthal distribution for the Grabowski vortex profile.

In this flow configuration, the vortex column undergoes three major types of breakdown to bubble, spiral, and double-helix modes. These modes are shown in Fig. 4 for the explicit calculation, where flow streaklines are superimposed on normalized pressure contours. The dark region indicates higher pressure and the light region indicates low pressure. As the major vortex structure is at the center of the computational domain,

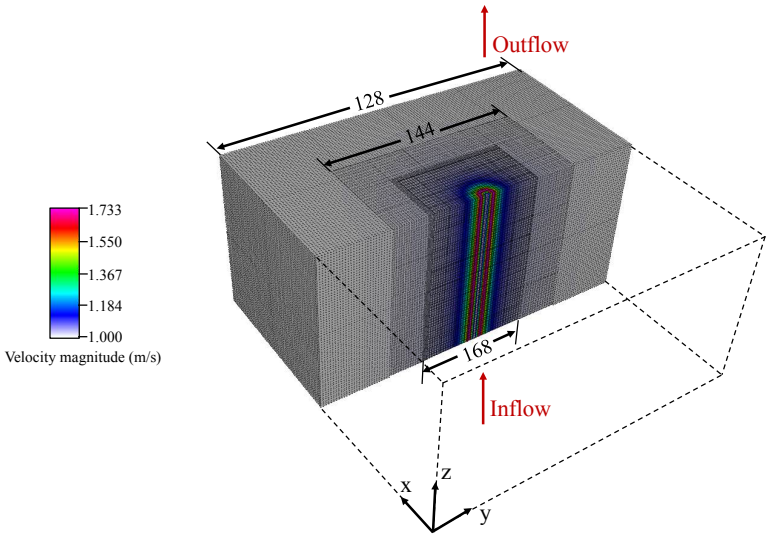

Figure 2. Computational domain and mesh with superimposed initial velocity field.

only the small, central section of the domain of 4 m × 20 m is shown in Fig. 4. They have been rotated 90° from that shown in Fig. 2, with the flow now going from left to right. The flow particle paths are visualized through streaklines by releasing massless particles at the inflow boundary from 18 locations distributed evenly along a circle centered at the vortex axis with a 5 cm radius. The particles released on the circle are colored as black, white and grey, which were selected to show different initial locations and the swirling motion. At the center of the vortex, the particles are colored pink. A schematic diagram of these particle injection points is shown in Fig. 3.

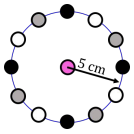

Figure 3. Layout of the particle injection location.

A comparison of the explicit and implicit calculations on the vortical structures of the three modes are shown in Figs. 5 and 6, corresponding to time $t = 146.6$ s and $t = 400.0$ s respectively. In these figures, the vortical structures are visualized by vorticity iso-surfaces with normalized vorticity magnitude $|\omega| = 0.5$. Figure 5 shows a bubble mode at an upstream location with a spiral mode downstream in both the explicit and implicit calculations. The location, shape, and size of the bubbles are very similar in these two calculations. The downstream spiral mode also shows agreement in the shape and length. The differences of the spiral motion, however, indicate a phase difference between the explicit and implicit calculations. At a later time, as shown in Fig. 6, the downstream spiral mode transitions into a double-helix mode in both cases. Similar to the phase difference of the spiral mode, this later time still shows a phase difference that affects the rotational motion of the double-helix mode. The upstream bubble, however, has a similar shape and size, as shown in Fig. 5.

A further comparison of the explicit and implicit calculations is then performed as a function of time to compare the time history of the transient flow development. This is done by extracting line profiles of the axial velocity and pressure along the axial centerline for all of the computational time steps and presenting them as z-t diagrams. We first compare the time history of the axial velocity profile and then the pressure development through the whole simulated period. Finally, the differences shown by the comparison lead us to focus on the first pressure wave propagation during the *initial* stages of flow development.

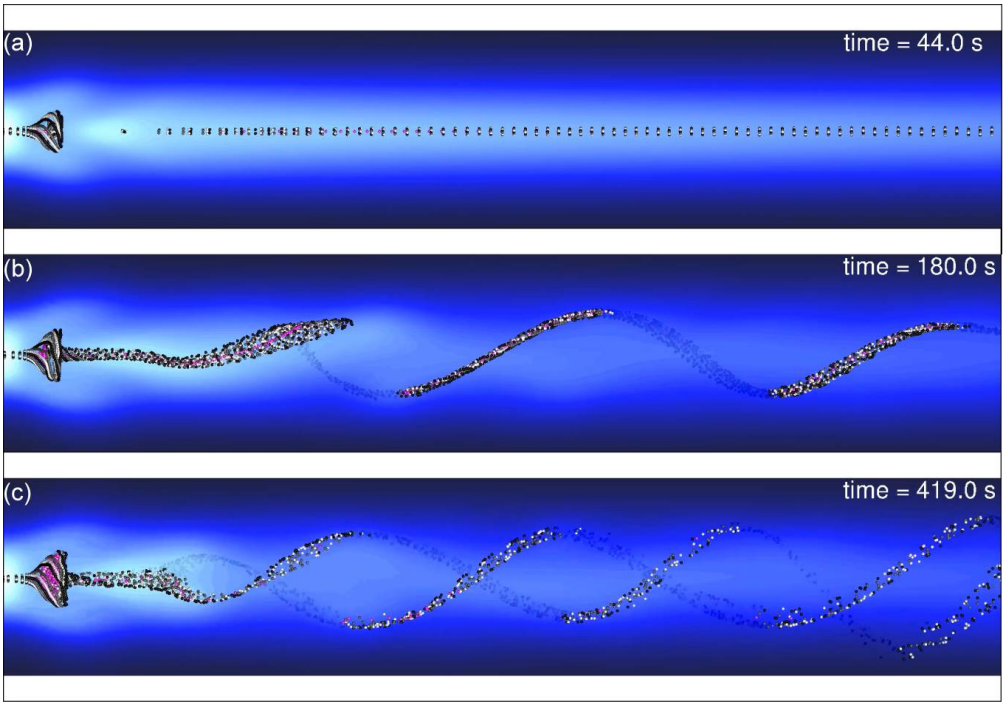

Figure 4. Streaklines imposed on contours of normalized pressure for the explicit FCT calculation with $CFL_{\mathbf{wave}} = 0.8$. The darker regions indicate higher pressure and the lighter regions indicate lower pressure. Time steps are selected to show the bubble mode, the spiral mode, and the double helix mode of vortex breakdown.

Figure 7 compares the axial velocity development along the vortex axis ($r = 0\,\mathrm{m}$) for the explicit and implicit simulations. We discuss this figure from bottom to top as time develops, and from left to right as from upstream to downstream. The flow is initialized with uniform axial velocity $v_z = 1\,\mathrm{m/s}$, and it slowly decays in magnitude. Not long after the start, we observe a small negative axial velocity region near the upstream inflow location, which lasts through out the entire time period. This regions corresponds to the bubble mode breakdown, as indicated by the arrow with a 'B' in Fig. 7 for both cases. Just downstream of the bubble, there is a small region with higher axial velocities, where the flow particles are injected out of the bubble with an acceleration into the downstream field. For both the explicit and implicit calculations, the results at this early stage from 0 s to about 110 s are similar. In Fig. 7a for the explicit calculation, from approximately 110 s to 220 s, oscillations form mainly due to the development of the downstream spiral mode and the transition from the spiral to the double-helix mode. At around 220 s, a second region with negative axial velocity forms downstream of the acceleration zone, which indicates the bifurcation point of the double-helix structure. The double-helix mode (H) is maintained through the rest of the simulation. For the implicit calculation in Fig. 7b, oscillations form after about 110 s due to the development of downstream secondary modes. The double-helix mode occurs at around 280 s for the implicit calculation.

Figure 8 compares the pressure development along the vortex axis ($r = 0\,\mathrm{m}$) for the explicit and implicit simulations. The pressure is normalized in both cases. We also discuss this from bottom to top as time develops, and from left to right as from upstream to downstream. For both cases, the time history of the pressure development is divided into three sections, as indicated by the white dashed lines and the numbers as section markers. Section 1 is an approximate time from when the upstream bubble mode starts to form to when it is fully developed (refer to Fig. 4a). Section 2 is an approximate time period when the downstream spiral mode forms (refer to Fig. 4b) and starts to transition into the double-helix mode. Section 3 is approximately when the there is a steady state double-helix mode downstream (refer to Fig. 4c).

In section 1, the pressure profile is initialized with a uniform distribution along the axial direction at the vortex center. The pressure starts to increase downstream near the outflow boundary due to the decay of the vortex. This creates an adverse pressure gradient along the axial direction, which imposes a force on the flow. When this force is so large that the momentum of the flow cannot overcome it, the vortex

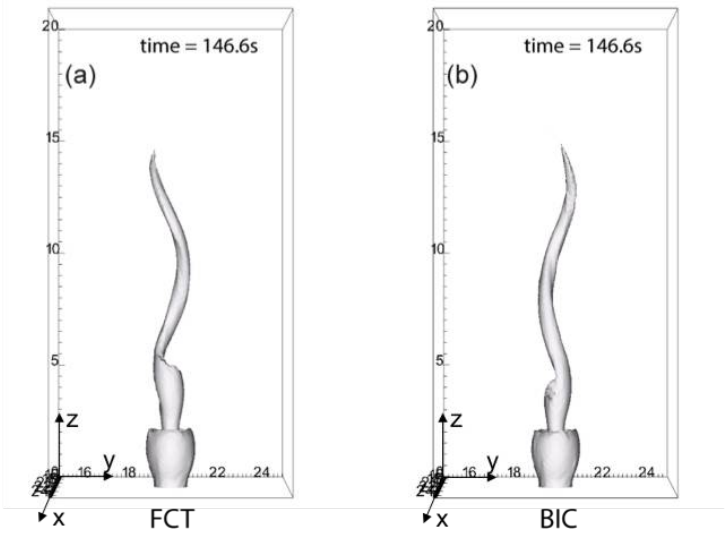

Figure 5. Vorticity iso-surface $|\omega| = 0.5$ for the explicit FCT and implicit BIC calculations with $CFL_{\mathbf{wave}} = 0.8$ at time $t = 146.6$ s. The vorticity magnitude is normalized by the maximum value. Only a central section of the computational domain is shown.

column breaks down into the bubble mode. The explicit FCT and implicit BIC results show a similar trend of this development of the pressure gradient. The strength of the gradient, however, is smaller in the implicit calculation compared to the explicit calculation.

In section 2, the high pressure regions grow larger towards the upstream direction, which is due to the blockage effect of the bubble. The oscillations shown have a relatively high frequency, which is associated with the motions of the spiral mode. More differences in the two calculations, however, exist in this time period. Here, there are two major oscillations with lower frequencies in Fig. 4b for the implicit simulation at approximately 160 s and 240 s, whereas in Fig. 4a for the explicit simulation, these oscillations are weaker with smaller amplitudes.

In section 3, the flow is fully developed and reaches a quasi-steady state, where we see a periodical oscillation in the pressure field with a relatively low frequency. This oscillation is also observed in Ref. 18, where they refer to it as a pulsating bubble state. The bubble empities and refills itself, thereby shrinking and growing in size periodically. In both the explicit and implicit calculations, the period of this oscillation is about 140 s, which is of the same order as observed in Ref. 18. The phase of this oscillation, however, is not synchronized in the explicit and implicit calculations. This is consistent with the phase shift in the helical flow structures in Fig. 6, which actually appears earlier in the spiral mode, as discussed before for Fig. 5. This is also consistent with the observations in Fig. 7, where there is an earlier development of the secondary instability development downstream in the explicit calculation than in the implicit one.

These phase differences between the explicit and implicit simulations of the spiral and helical modes now lead us to look at the beginning of the simulations to determine the cause of the asynchronization. We therefore focus on the first 20 s of the calculations. In order to better visualize the pressure wave propagation along the axial direction, we take the same datasets used in Fig. 8 and normalize them by applying $P(z,t_i) = \frac{P(z,t_i) - \text{mean}(P(z,t_i))}{\text{mean}(P(z,t_i))}$ for all time steps t_i. The results for the first 20 s are shown in Fig. 9 for both calculations. The black dashed lines indicate the first major pressure wave propagation from upstream to downstream. Below the black dashed lines, the flow corresponds to times at which has not yet felt the pressure wave coming from upstream, where the pressure increases with a uniform rate across the axial locations due to the vortex dissipation. For regions above the black dashed lines and below around 10s, the flow has felt the pressure wave traveling downstream, but the wave has not reached the outflow boundary and reflected back. Due to the wave effect, the pressure in this region increases with a different rate as before. There is a time delay at different axial locations of this change of rate, since the wave propagates at a finite speed. In general, the regions before 10 s in both calculations show strong agreement with each other. After the wave interacts with the outflow boundary, there is a clearer difference in the pressure between the explicit

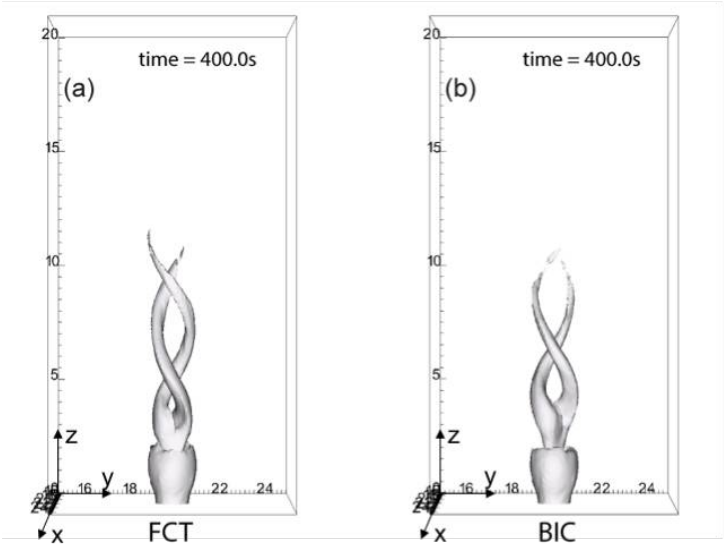

Figure 6. Vorticity iso-surface $|\omega| = 0.5$ for the explicit FCT and implicit BIC calculations with $CFL_{\mathbf{wave}} = 0.8$ at time $t = 400.0$ s. The vorticity magnitude is normalized with the maximal value. Only a central section of the computational domain is shown.

and implicit simulations. In this figure, the differences mainly show up near the outflow boundary, where the pressure is higher in the explicit calculation than in the implicit one. This leads us to speculate that it is the difference between how the explicit FCT and implicit BIC are related to the outflow boundary condition that causes the difference in the pressure field, and further affects the phase of the instabilities.

To confirm this, we extract the time history of pressure from Fig. 8 at axial locations $z = 10\,\mathrm{m}$ and $z = 20\,\mathrm{m}$ for the first 30 s and compare them in Fig. 10 for both cases. In this figure, we go from the left to the right as advancing in time, and discuss the three important time stages that are marked as A, B, and C. From the beginning to time A, the pressure wave travels from upstream to downstream before reaching $z = 10\,\mathrm{m}$. The pressure at $z = 10\,\mathrm{m}$ and $z = 20\,\mathrm{m}$ both rises with a same rate due to the uniform vortex dissipation, as discussed above. Note that the explicit and implicit results agree very well at both locations. At time A, the pressure wave arrives at $z = 10\,\mathrm{m}$, therefore the slope of the pressure profile at $z = 10\,\mathrm{m}$ changes due to the wave influence. At this time, no significant changes occur in the rate of the pressure increase at $z = 20\,\mathrm{m}$. From time A to time B, the pressure wave is traveling from $z = 10\,\mathrm{m}$ to $z = 20\,\mathrm{m}$ before it reaches the boundary, during which the explicit and implicit results maintain strong agreements at both axial locations. At time B, the pressure wave arrives at $z = 20\,\mathrm{m}$, which is at the outflow boundary. Similarly, the slope of the pressure profile for $z = 20\,\mathrm{m}$ changes under the wave effect.

A deviation of the BIC curve from the FCT curve at $z = 20\,\mathrm{m}$, however, occurs when this wave interacts with the boundary and reflection effects start to occur in the domain. This deviation results in a growing discrepancy between the BIC and FCT results as the time grows. From time B, the influence from the outflow boundary starts to propagate back into the domain. Note that before it reaches $z = 10\,\mathrm{m}$ at time C, the explicit and implicit results at $z = 10\,\mathrm{m}$ follow closely with each other over time. Once it passes $z = 10\,\mathrm{m}$ after time C, we observe a similar deviation between the two calculations at $z = 10\,\mathrm{m}$ as time grows. The discrepancy is smaller compared with that at $z = 20\mathrm{m}$, but at both locations, the explicit calculation predicts a larger pressure gradient than that from the implicit calculation.

This larger pressure gradient downstream of the bubble may be the main reason that causes the secondary instabilities (the spiral and the double-helix modes) to occur earlier than in the implicit calculation, which is essentially the origin of the phase difference in the downstream motions discussed above. This discrepancy is essentially from the difference of how the implicit algorithm handles the open outflow boundary through an elliptic solver, versus the explicit algorithm by using an explicit FCT solver. Note that the flow upstream of the bubble is not affected by this pressure wave difference. This to some extent confirms that the bubble mode is a critical state in which no waves can propagate further upstream, and which separates the flow from an upstream supercritical state to a downstream subcritical state.

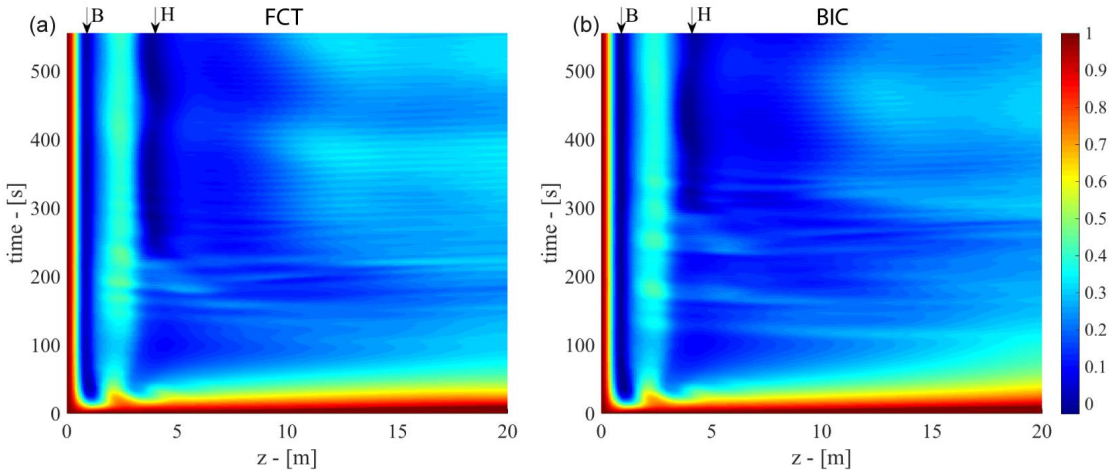

Figure 7. Time history of the axial velocity v_z along the vortex axis ($r = 0\,\mathrm{m}$) for the explicit FCT and implicit calculations with $CFL_{\mathbf{wave}} = 0.8$. The arrow with 'B' indicates the location of the bubble mode, and the arrow with 'H' indicates the location of the bifurcation point of the double-helix mode.

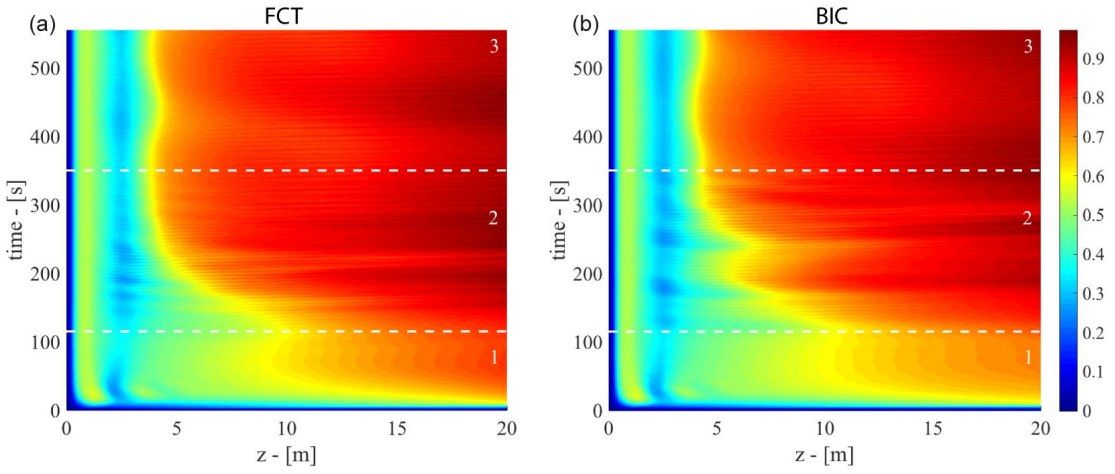

Figure 8. Time history of the normalized pressure along the vortex axis ($r = 0\,\mathrm{m}$) for the explicit FCT and implicit calculations with $CFL_{\mathbf{wave}} = 0.8$. The time history is divided into three sections based on the flow development indicated by the white dashed lines and the associated numbers.

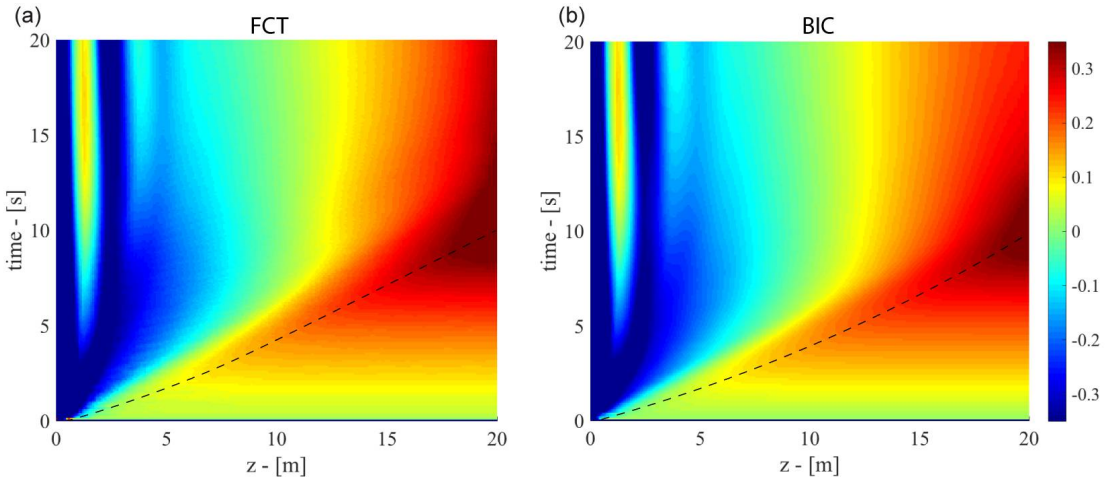

Figure 9. Time history of the pressure along the vortex axis ($r = 0\,\mathrm{m}$) normalized by $P(z,t_i) = \frac{P(z,t_i) - \mathbf{mean}(P(z,t_i))}{\mathbf{mean}(P(z,t_i))}$ for all time steps t_i, for the explicit FCT and implicit calculations with $CFL_{\mathbf{wave}} = 0.8$. The black dashed lines indicate the approximate propagation paths of the first major pressure wave.

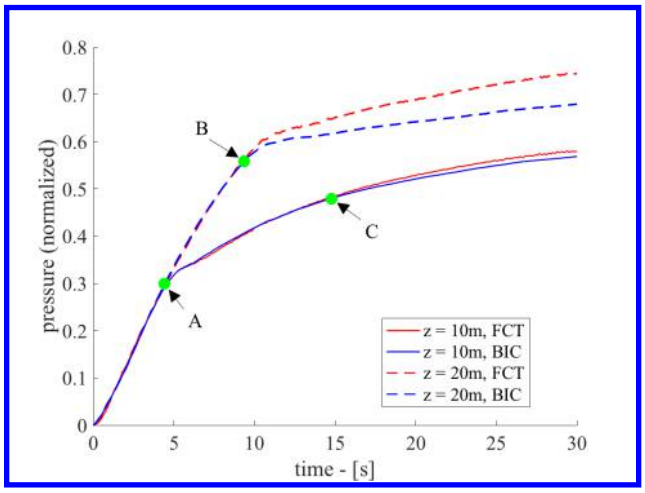

Figure 10. Normalized pressure extracted at two locations: (1) radial location $r = 0\,\mathrm{m}$, axial location $z = 10\,\mathrm{m}$, and (2) radial location $r = 0\,\mathrm{m}$, axial location $z = 20\,\mathrm{m}$ for the first 30 seconds from both explicit FCT and implicit BIC calculations with $CFL_{\mathbf{wave}} = 0.8$.

V. Conclusion

In this work, we simulated three-dimensional compressible vortex breakdown using both the explicit FCT algorithm and an implicit algorithm, called BIC-FCT. In a previous publication,[33] we demonstrated BIC's performance on predicting the major types of vortex breakdown using large implicit time steps without the sound-speed restriction. Then we compared the results with an explicit calculation using small time steps within the explicit stability limit. Here we described a direct comparison between the explicit and implicit calculations by adopting the exact same time steps within the explicit stability limit, and the same diffusion fluxes integration in both methods.

The comparison shows a good qualitative agreement between the two simulations on the location and shape of the bubble mode and the size and shape of the spiral and the double-helix modes. There are, however, differences in the onset time of the downstream double-helix mode and the phase of the rotating motions of the spiral and the double-helix modes.

To investigate the origin of these differences, we compared line profiles of the axial velocity and the pressure along the axial centerline over time. This analysis shows a pressure wave propagating from inflow to outflow during the first 20 s of the simulations. The explicit and implicit calculations follow each other closely until this wave reaches and interacts with the outflow boundary. Then the two calculations start to deviate once the reflection propagates from the outflow boundary into the upstream flow. There is a time delay for this deviation at different axial locations, since the reflected waves propagate at finite speeds. At each axial location the reflected wave passes, the explicit calculation predicts a larger pressure gradient than that in the implicit calculation. This discrepancy is the origin of the phase shift of the spiral and the double-helix modes in the two calculations.

The source of this discrepancy is from the difference in how the implicit algorithm is coupled to the open outflow boundary through an elliptic solver versus the explicit algorithm by using an explicit FCT solver. This downstream wave discrepancy does not cause a difference of the behavior of the bubble mode in both simulations, which is consistent with the theory that breakdown represents a transition in the flow from supercritical to subcritical state.

Acknowledgments

This work was supported by the Army Research Office (grant W911NF1710524) and by the National Science Foundation under award CBET 1839510. This work was also supported in part by the University of Maryland through Minta Martin Endowment Funds in the Department of Aerospace Engineering, and through the Glenn L. Martin Institute Chaired Professorship and the A. James Clark Distinguished Professorship at the A. James Clark School of Engineering. Computations were performed using the University of Maryland Deepthought2 HPC cluster and the Air Force Research Laboratory's Thunder. The second author is grateful to Dr. Vadim Gamezo and the Laboratory of Computational Physics, Naval Research Laboratory (NRL), for providing the DoD supercomputing resources to access Thunder.

References

[1]Sarpkaya, T., "On Stationary and Travelling Vortex Breakdowns," *Journal of Fluid Mechanics*, Vol. 45, No. 3, 1971, pp. 545–559.

[2]Sarpkaya, T., "Vortex Breakdown in Swirling Conical Flows," *AIAA J*, Vol. 9, No. 9, 1971, pp. 1792–1799.

[3]Leibovich, S., "The Structure of Vortex Breakdown," *Annual Review of Fluid Mechanics*, Vol. 10, No. 1, 1978, pp. 221–246.

[4]Billant, P., Chomaz, J.-M., and Huerre, P., "Experimental Study of Vortex Breakdown in Swirling Jets," *Journal of Fluid Mechanics*, Vol. 376, 1998, pp. 183–219.

[5]Hall, M., "A New Approach to Vortex Breakdown," *Proc. Heat Transfer Fluid Mech. Inst*, 1967, pp. 319–340.

[6]Squire, H., *Analysis of the Vortex Breakdown Phenomenon*, Imperial College of Science and Technology, Aeronautics Department, 1960.

[7]Benjamin, T. B., "Theory of the Vortex Breakdown Phenomenon," *Journal of Fluid Mechanics*, Vol. 14, No. 4, 1962, pp. 593–629.

[8]Jones, J., *The Breakdown of Vortices in Separated Flow*, University of Southampton, Department of Aeronautics & Astronautics, 1960.

[9]Ludwieg, H., *Zur Erklärung der Instabilität der über angestellten Deltaflügeln auftretenden freien Wirbelkerne*, Aerodynamische Versuchsanstalt, 1962.

[10]Howard, L. N. and Gupta, A., "On the Hydrodynamic and Hydromagnetic Stability of Swirling Flows," *Journal of Fluid Mechanics*, Vol. 14, No. 3, 1962, pp. 463–476.

[11]Spall, R. E., Gatski, T. B., and Grosch, C. E., "A Criterion for Vortex Breakdown," *The Physics of fluids*, Vol. 30, No. 11, 1987, pp. 3434–3440.

[12]Brown, G. and Lopez, J., "Axisymmetric Vortex Breakdown Part 2. Physical Mechanisms," *Journal of Fluid Mechanics*, Vol. 221, 1990, pp. 553–576.

[13]Escudier, M., "Confined Vortices in Flow Machinery," *Annual Review of Fluid Mechanics*, Vol. 19, No. 1, 1987, pp. 27–52.

[14]Escudier, M. and Keller, J., "Vortex Breakdown: a Two-stage Transition," Tech. rep., BROWN BOVERI RESEARCH CENTER BADEN (SWITZERLAND), 1983.

[15]Hall, M., "Vortex Breakdown," *Annual review of fluid mechanics*, Vol. 4, No. 1, 1972, pp. 195–218.

[16]Grabowski, W. J. and Berger, S., "Solutions of the Navier-Stokes Equations for Vortex Breakdown," *Journal of Fluid Mechanics*, Vol. 75, No. 3, 1976, pp. 525–544.

[17]Spall, R., Gatski, T., and Ash, R., "The Structure and Dynamics of Bubble-type Vortex Breakdown," *Proceedings of the Royal Society of London A: Mathematical, Physical and Engineering Sciences*, Vol. 429, The Royal Society, 1990, pp. 613–637.

[18]Ruith, M., Chen, P., Meiburg, E., and Maxworthy, T., "Three-dimensional Vortex Breakdown in Swirling Jets and Wakes: Direct Numerical Simulation," *Journal of Fluid Mechanics*, Vol. 486, 2003, pp. 331–378.

[19]Melville, R., "The Role of Compressibility in Free Vortex Breakdown," *Fluid Dynamics Conference*, 1996, p. 2075.

[20]Luginsland, T., *Numerical Investigation of Vortex Breakdown in Compressible, Swirling Nozzle-jet Flows*, Ph.D. thesis, 2014.

[21]Rusak, Z., Choi, J. J., Bourquard, N., and Wang, S., "Vortex Breakdown of Compressible Subsonic Swirling Flows in a Finite-length Straight Circular Pipe," *Journal of Fluid Mechanics*, Vol. 781, 2015, pp. 3–27.

[22]Huang, Y. and Yang, V., "Effect of Swirl on Combustion Dynamics in a Lean-premixed Swirl-stabilized Combustor," *Proceedings of the Combustion Institute*, Vol. 30, No. 2, 2005, pp. 1775–1782.

[23]Duwig, C. and Fuchs, L., "Large Eddy Simulation of Vortex Breakdown/Flame Interaction," *Physics of Fluids*, Vol. 19, No. 7, 2007, pp. 075103.

[24]MacCormack, R. W., "A Numerical Method for Solving the Equations of Compressible Viscous Flow," *AIAA journal*, Vol. 20, No. 9, 1982, pp. 1275–1281.

[25]Fryxell, B. A., Woodward, P. R., Colella, P., and Winkler, K.-H., "An Implicit-explicit Hybrid Method for Lagrangian Hydrodynamics," *Journal of Computational Physics*, Vol. 63, No. 2, 1986, pp. 283–310.

[26]Yee, H. and Harten, A., "Implicit TVD Schemes for Hyperbolic Conservation Laws in Curvilinear Coordinates," *AIAA journal*, Vol. 25, No. 2, 1987, pp. 266–274.

[27]Jones, W. W. and Boris, J. P., "Flame and Reactive Jet Studies Using a Self-consistent Two-dimensional Hydrocode," *The Journal of Physical Chemistry*, Vol. 81, No. 25, 1977, pp. 2532–2534.

[28]Rehm, R. and Baum, H., "The Equations of Motion for Thermally Driven, Buoyant Flows," *Journal of Research of the NBS*, Vol. 83, 1978, pp. 297–308.

[29]Paolucci, S., *Filtering of Sound from the Navier-Stokes Equations*, Sandia National Laboratories Livermore, CA, 1982.

[30]Pember, R. B., Howell, L. H., Bell, J. B., Colella, P., Crutchfield, W. Y., Fiveland, W., and Jessee, J., "An Adaptive Projection Method for Unsteady, Low-Mach Number Combustion," *Combustion Science and Technology*, Vol. 140, No. 1-6, 1998, pp. 123–168.

[31]Nicoud, F., "Conservative High-order Finite-difference Schemes for Low-Mach Number Flows," *Journal of Computational Physics*, Vol. 158, No. 1, 2000, pp. 71–97.

[32]Thornber, B., Mosedale, A., Drikakis, D., Youngs, D., and Williams, R. J., "An Improved Reconstruction Method for Compressible Flows with Low Mach Number Features," *Journal of computational Physics*, Vol. 227, No. 10, 2008, pp. 4873–4894.

[33]Zhang, X., Chung, J. D., Kaplan, C. R., and Oran, E. S., "The Barely Implicit Correction Algorithm for Low-Mach-Number Flows," *Computers & Fluids*, Vol. 175, 2018, pp. 230–245.

[34]Patnaik, G., Guirguis, R., Boris, J., and Oran, E., "A Barely Implicit Correction for Flux-corrected Transport," *Journal of Computational Physics*, Vol. 71, No. 1, 1987, pp. 1–20.

[35]Patnaik, G., Laskey, K., Kailasanath, K., Oran, E., and Brun, T., "FLIC - A detailed, two-dimensional flame model," *NRL Memorandum report*, Vol. 6555, 1989.

[36]Boris, J. P., Landsberg, A. M., Oran, E. S., and Gardner, J. H., "LCPFCT- a Flux-corrected Transport Algorithm for Solving Generalized Continuity Equations," Tech. rep., NAVAL RESEARCH LAB WASHINGTON DC, 1993.

[37]Zalesak, S. T., "Fully Multidimensional Flux-corrected Transport Algorithms for Fluids," *Journal of computational physics*, Vol. 31, No. 3, 1979, pp. 335–362.

[38]DeVore, C. R., "An Improved Limiter for Multidimensional Flux-corrected Transport," Tech. rep., NAVAL RESEARCH LAB WASHINGTON DC, 1998.